Eulerian-Eulerian two-fluid model for laminar bubbly pipe flows: validation of the baseline model

Liao, Y.; Upadhyay, K.; Schlegel, F.;

Originally published:

April 2020

Computers & Fluids 202(2020), 104496

DOI: https://doi.org/10.1016/j.compfluid.2020.104496

Perma-Link to Publication Repository of HZDR:

https://www.hzdr.de/publications/Publ-29438

Eulerian-Eulerian two-fluid model for laminar bubbly pipe flows: validation of the baseline model

Yixiang Liao*, **Kartik Upadhyay** and **Fabian Schlegel**

Helmholtz-Zentrum Dresden-Rossendorf, Institute of Fluid Dynamics, Bautzner Landstraße 400, 01328 Dresden, Germany

Abstract

In the present paper, an Euler-Euler two-fluid model combined with the baseline model, which is a set of closures for the interfacial momentum and turbulence transfer, is validated against experimental data for low Reynolds number bubbly flows in vertical pipes. The model has already been validated for high Reynolds number pipe flows and bubble columns in the previous work (Liao et al., 2019, Chem. Eng. Sci. 202, 55-69). To further substantiate the $k-\omega$ SST model with consideration of bubble-induced source included in the baseline model, it is of interest to examine it for low Reynolds number pipe flows, where the bulk is laminar and the transition to turbulence is induced sorely by the agitation of bubbles. Simulations are configured and carried out in the open source CFD code OpenFOAM for eight test cases. Each of them has a different combination of gas and liquid volumetric flow rates. The numerical results are then compared with the experimental data taken from the literature. The comparison is based on different parameters including air void fraction, mean bubble velocity, mean liquid velocity, turbulent kinetic energy and Reynolds shear stress. Although, mostly, confirming results with the experimental data are presented but further improvement of the model for turbulent transition as well as inter-phase momentum transfer is necessary. Reliable prediction of velocity profile in single-phase and extremely sparse bubbly flow cases is shown, and the phase distribution in fully-developed cases is well captured. In addition to the bulk Reynolds and void fraction, the pipe-to-bubble size ratio is found to have definite influence on the laminar-turbulent transition.

Keywords: Baseline model, Bubbly flows, Bubble-induced turbulence, Low-Re (Reynolds) flows, OpenFOAM.

1 Introduction

The application of bubbly flows is an important and interesting topic. Many industries and disciplines involve bubbly flows e.g. power plants, automotive, chemical, biological etc., getting benefited from their high mixing properties and large heat, momentum and mass transfer area. The importance of bubbly flows is making researchers focus on this topic even more and postulate general modeling concepts regarding the motion and phase distribution of the two-phase mixture that govern the transfer processes. Flows generated by injecting bubbles into laminar bulk flow exhibit clear turbulence characteristics and higher mixing rates than single-phase flows with similar bulk Reynolds number. Actually, understanding how the bubbles bring the laminar Poiseuille flow to fully developed turbulence is still not achieved. Modeling of the bubble-induced turbulence ("pseudo-turbulence") represents still a major scientific challenge due to its different generation and dissipation mechanism as well as the present empiricism in single-phase turbulence modeling. Some scientists and researchers have performed experiments to investigate the phase distribution and turbulence structures in such kind of flow conditions (Nakoryakov et al. , 1996; Hosokawa and Tomiyama , 2013; Kim et al. , 2016) and uncommon phenomena were observed. For example, the experiments conducted by Hosokawa and Tomiyama (2013) evidence that bubbles having a size larger than 3.5 mm migrate to the pipe center and form a clear core-peak profile in upward flows, whereas the common value for high Re air-water flows under normal conditions is found to be around 5.6 mm by Tomiyama (2002) and Lucas and Tomiyama (2011). Although reasonable

*Corresponding author: y.liao@hzdr.de

explanations for the flow characteristics are not yet available, it indicates that the models used for the simulation of high Reynolds number bubbly flows may not be suitable for these "laminar" cases. A preliminary comparative study is necessary, whereas little attention has been paid to these concerns, namely the laminar-turbulent transition in bubbly flows. Matas et al. (2003) investigated experimentally the influence of neutrally-buoyant suspended particles on the transition to turbulence, and found that the role of particles depend on their concentration and the pipe-to-particle diameter ratios, and the transition was delayed at large pipe-to-particle diameter ratios. To the authors' knowledge, research on the influence of bubbles in bubbly flow is not available.

Computational fluid dynamics (CFD) provides high-resolved, inexpensive and efficient solutions of flow field equations under a variety of situations. It assists in understanding the transition from laminar to turbulence in bubbly flow due to the injection of bubbles. The Euler-Euler CFD approach with the RANS (Reynolds-Averaged Navier-Stokes) equations for turbulence modeling is so far the most widely used tool for practical purposes due to low computational costs. However, the accuracy and reliability of the simulation results is still largely degraded by insufficient understanding of local physical phenomena, e.g. inter-phase momentum and turbulence transfer, which has to be specified with aid of closure models. For each of the phenomena many models exist with different range of validity. The diversity and uncertainty contained in the closures prevent the community from establishing best practices guidelines regarding model selection for CFD simulations of bubbly flows. Simulation and validation results are hardly ever comparable across researcher groups. To improve the situation, a few years ago, HZDR presented a baseline model strategy with fixed models and numerical setups, as far as possible, for the simulation of various bubbly flows (Lucas et al. , 2016). It aims to unveil the physical laws that are missing in the numerical models but covered by artificial tuning, and thereby contributes to developing more general ones. Various papers have been published regarding the validation of the baseline model for high liquid Re flows, e.g. Liao et al. (2015, 2018, 2019), Liao and Lucas (2016), Rzehak et al. (2017) and Kriebitzsch and Rzehak (2016), and to extend the applications, it is being evaluated and compared for low Re bubbly flows in this paper. As an overview, the Euler-Euler CFD simulations are performed with the baseline model and validated against the experiments performed by Hosokawa and Tomiyama (2013), Kim et al. (2016) in OpenFOAM. Various parameters like gas void fraction, mean liquid and bubble velocity, turbulent kinetic energy or root mean square velocity fluctuations are compared and a general observation is presented.

The paper is organized as follows. In section 2, we briefly describe the mathematical models adopted, with their implementation in OpenFOAM like numerics etc. Section 3, gives an outlook regarding the experimental setup and conditions and how the test cases are set-up. Consequently, section 4 provides an insight for the geometry, boundary conditions, solver settings and pre-processing that is used for our simulations. Following this, section 5 presents the comparison results between the experimental data and simulations and also outlines precision of numerical models. Finally, in Section 6, we have summarized with conclusions based on our observations and specific remarks for certain behavior which leaves future scope for improvements and making the model more accurate.

2 Models Description

In the following section, a brief explanation is presented for the mathematical models involved in the simulation set-up. In addition, the algorithm used in OpenFOAM is also described.

2.1 Mathematical

The most important equations for isothermal fluid flows comprised of the continuity equation and the Navier-Strokes equation for resolving the flow characteristics in a domain. As mentioned above the Euler-Euler two-fluid formulation of these conservation equations has been adopted in the present work. The information about momentum as well as turbulence transfer across the interface is reconstructed with aid of the baseline model (Lucas et al. , 2016; Liao et al. , 2018).

2.1.1 Conservation equations

The conservation of mass for isothermal flows (without external sources and interfacial mass transfer) can be written as:

$$\frac{\partial \alpha_{\mathrm{G}} \rho_{\mathrm{G}}}{\partial \mathrm{t}} + \nabla \cdot (\alpha_{\mathrm{G}} \rho_{\mathrm{G}} \boldsymbol{u}_{\mathrm{G}}) = 0 \text{ and } \frac{\partial \alpha_{\mathrm{L}} \rho_{\mathrm{L}}}{\partial \mathrm{t}} + \nabla \cdot (\alpha_{\mathrm{L}} \rho_{\mathrm{L}} \boldsymbol{u}_{\mathrm{L}}) = 0. \tag{1}$$

Here, subscript G denotes for the gas phase and L denotes for the liquid phase, where $\alpha_{\mathrm{L}} + \alpha_{\mathrm{G}} = 1$. Similarly, the momentum conservation equation for the two phases is written respectively as:

$$\frac{\partial (\alpha_G \rho_G \boldsymbol{u}_G)}{\partial t} + \nabla \cdot (\alpha_G \rho_G \boldsymbol{u}_G \times \boldsymbol{u}_G) = -\alpha_G \nabla p + \nabla \cdot (\alpha_G \boldsymbol{T}_G) + \alpha_G \rho_G \boldsymbol{g} + \boldsymbol{F}_G^{inter}, \tag{2}$$

$$\frac{\partial (\alpha_L \rho_L \boldsymbol{u}_L)}{\partial t} + \nabla \cdot (\alpha_L \rho_L \boldsymbol{u}_L \times \boldsymbol{u}_L) = -\alpha_L \nabla p + \nabla \cdot (\alpha_L \boldsymbol{T}_L) + \alpha_L \rho_L \boldsymbol{g} + \boldsymbol{F}_L^{inter}. \tag{3}$$

Here, $\mathbf{T}$ denotes the stress tensor and contains viscous and Reynolds stress terms, and the Reynolds shear stress is determined according to the Boussinesq eddy viscosity assumption.

$$\tau_{\mathrm{ij}} = 2\nu_{\mathrm{t}} \mathrm{S}_{\mathrm{ij}} - \frac{2}{3} \rho \mathrm{k} \delta_{\mathrm{ij}}, \tag{4}$$

where, ν_t is the turbulent viscosity. The vector $\mathbf{F}$ denotes the forces that act at the interfaces in a two-phase system governing the interfacial momentum transfer. It can be decomposed into several components. The following different forces are accounted for in the present work;

$$\boldsymbol{F}_G^{inter} = -\boldsymbol{F}_L^{inter} = \boldsymbol{F}^{drag} + \boldsymbol{F}^{lift} + \boldsymbol{F}^{wall} + \boldsymbol{F}^{disp} + \boldsymbol{F}^{vm} \tag{5}$$

where,

- $\mathrm{F}^{\mathrm{drag}}$ denotes the overall inter-phase drag force due to relative motion including both skin friction and form drag;
- $\mathrm{F}^{\mathrm{lift}}$ denotes the shear lift force due to the mean flow gradient and inertia effects, which acts perpendicularly to the direction of relative motion. It may have negative and positive sign depending on bubble size and leads to the demixing motion of large and small bubbles;
- $\mathrm{F}^{\mathrm{wall}}$ denotes the wall lubrication force, which describes the lateral migration of bubbles due to the presence of wall, always points away from the wall and prevents bubbles from penetrating the wall;
- $\mathrm{F}^{\mathrm{disp}}$ denotes the turbulent dispersion force accounting for the inter-phase turbulent momentum transfer, which acts as a turbulent diffusion in dispersed bubbly flows, proportional to void fraction gradients and has a smoothing effect on the profile;
- F^{vm} denotes the virtual mass force, which describes the liquid mass carried by bubbles as they flow faster than the liquid, and is significant when the gas density is much smaller than the liquid density.

2.1.2 Closures for bubble forces

For the closure of the interfacial forces mentioned above, many models exist for each force with different ranges of validity. To minimize uncertainties regarding model selection, the models prescribed in the baseline setup are adopted (Liao et al. , 2019). It is worth emphasizing that application of the baseline model is without claim of its completeness and perfectness. It severs as a basis for reasonable comparison of the simulation results across different cases, e.g. turbulent and laminar bubbly flows. For more details about the baseline model readers could refer to Lucas et al. (2016), Liao and Lucas (2016), Liao et al. (2015, 2018), Kriebitzsch and Rzehak (2016) and Rzehak et al. (2017). The inter-phase drag force is modeled by the following general form

$$\boldsymbol{F}^{\mathrm{drag}} = -\frac{3\mathrm{C_D}}{4} \frac{\rho_{\mathrm{L}} \alpha_{\mathrm{G}}}{\mathrm{d_B}} |\boldsymbol{u}_{\mathrm{G}} - \boldsymbol{u}_{\mathrm{L}}| (\boldsymbol{u}_{\mathrm{G}} - \boldsymbol{u}_{\mathrm{L}}) \tag{6}$$

where d_B is the bubble diameter assumed constant in this work according to the experimental conditions, and C_D is an overall drag coefficient, for which a closure model is required. The

following correlation suggested by Ishii and Zuber (1979) for sparse bubbly flow is adopted, which distinguishes different bubble shapes as:

$$\mathrm{C_D} = \max(\mathrm{C_{D,sphere}},\ \min(\mathrm{C_{D,ellipse}}, \mathrm{C_{D,cap}})) \text{ with,} \tag{7a}$$

$$\mathrm{C_{D,sphere}} = \frac{24}{\mathrm{Re_p}}(1 + 0.1\mathrm{Re_p^{0.75}}) \tag{7b}$$

$$\mathrm{C_{D,ellipse}} = \frac{2}{3}\sqrt{\mathrm{Eo}} \tag{7c}$$

$$\mathrm{C_{D,cap}} = \frac{8}{3} \tag{7d}$$

where Re_p denotes the particle Reynolds number and Eo denotes Eötvös number. The expression for the shear-induced lift force acting on the dispersed bubbles in the presence of rotational liquid was first obtained by Saffman (1965),

$$\boldsymbol{F}^{\mathrm{lift}} = -\mathrm{C_L}\rho_\mathrm{L}\alpha_\mathrm{G}(\boldsymbol{u}_\mathrm{G} - \boldsymbol{u}_\mathrm{L}) \times (\nabla \times \boldsymbol{u}_\mathrm{L}). \tag{8}$$

The non-dimensional lift coefficient C_L is estimated using the correlation proposed by Tomiyama et al. (2002). Like the Ishii-Zuber drag force model (Ishii and Zuber , 1979), it is applicable for different bubble shape regimes, and depends on the modified Eötvös number,Eo_d, which is defined by using the maximum horizontal dimension of a bubble as a characteristic length.

$$C_L = \begin{cases} \min[0.288\tanh(0.121\mathrm{Re_b}),\ \mathrm{f(Eo_d)}] & \mathrm{Eo_d} < 4. \\ \mathrm{f(Eo_d)} & 4 < \mathrm{Eo_d} < 10 \\ -0.27 & \mathrm{Eo_d} > 10 \end{cases} \tag{9}$$

$$\mathrm{f(Eo_d)} = 0.00105\mathrm{Eo_d^3} - 0.0159\mathrm{Eo_d^2} - 0.0204\mathrm{Eo_d} + 0.474\,. \tag{10}$$

The important feature of the Tomiyama lift force model is prediction of the cross-over point in bubble size (or critical bubble size) at which bubble deformation causes a reversal of the sign of the lift force to take place. The point plays a crucial role in determining void distributions. By approximating the bubble aspect ratio using the Wellek correlation (Wellek et al. , 1966) for spheroidal bubbles in a fully contaminated system, Tomiyama et al. (2002) found the value to be around $5.6\,mm$ for air-water dispersed systems under normal conditions. It should be noted that the bubble shape and thus the cross-over bubble size in investigated cases may deviate from the approximation due to various degree of contamination, but the information for a precise definition is unavailable.

Both numerically and experimentally it is confirmed that the presence of a wall has a significant effect on the lateral migration of bubbles in the vicinity. However, due to the complexity, knowledge on hydrodynamic interactions close to the wall is quite limited, which prevents CFD simulations from a reliable prediction in this region. The baseline model recommends the work of Hosokawa et al. (2002), who modified the wall lubrication force formulation of Antal et al. (1991)

$$\boldsymbol{F}^{\mathrm{wall}} = -\frac{\mathrm{d_B}}{2}\frac{1}{\mathrm{y_W^2}}\mathrm{C_W}\rho_\mathrm{L}\alpha_\mathrm{G}|\boldsymbol{u}_\mathrm{G} - \boldsymbol{u_L}|^2\hat{\boldsymbol{y}}, \tag{11}$$

where d_B is bubble diameter and $\hat{\boldsymbol{y}}$ is a unit normal vector pointing away from the pipe wall and y_W is the distance to the nearest wall. A correlation for the coefficient C_W was obtained by correlating the experimental data for bubble trajectories in the vicinity of a vertical flat wall. It was found that for large deformed bubbles ($Re_p \geq 10$) C_W is well correlated with the Eötvös number Eo

$$\mathrm{C_W} = 0.0217\,\mathrm{Eo}\,. \tag{12}$$

The inclusion of turbulence dispersion force is to account for additional diffusion effects due to turbulent fluctuations. It results in dispersion of bubbles from high volume fraction regions to low volume fraction regions, and thus has a smoothing effect on the void distributions. The model derived by Burns et al. (2001) on the basis of the Favre average of the inter-phase drag force is used in this work.

$$\boldsymbol{F}^{\mathrm{disp}} = -\mathrm{C_{TD}}\frac{3}{4}\mathrm{C_D}\frac{\rho_\mathrm{L}\alpha_\mathrm{G}}{\mathrm{d_B}}|\boldsymbol{u}_\mathrm{G} - \boldsymbol{u}_\mathrm{L}|\frac{\mu_\mathrm{L}^{\mathrm{turb}}}{\sigma_\mathrm{tc}}\left(\frac{1}{\alpha_\mathrm{L}} + \frac{1}{\alpha_\mathrm{G}}\right)\nabla\alpha_\mathrm{G}, \tag{13}$$

where C_{TD} is a user-modifiable constant, which is fixed at the value of 1.0 according to the baseline model and the turbulent Schmidt number for continuous phase, σ_{tc}, is set to be 0.7. The virtual mass force acting on the bubble is

$$\boldsymbol{F}^{\mathrm{vm}} = -\mathrm{C_{VM}}\rho_{\mathrm{L}}\alpha_{\mathrm{G}}(\frac{\mathrm{D_G}\boldsymbol{u}_{\mathrm{G}}}{\mathrm{Dt}} - \frac{\mathrm{D_L}\boldsymbol{u}_{\mathrm{L}}}{\mathrm{Dt}}), \tag{14}$$

where $^{D_G}/_{Dt}$ and $^{D_L}/_{Dt}$ denotes the material derivative with respect to the gas and liquid velocity, respectively. The virtual mass coefficient C_{VM} may depend on bubble shape and concentration as well as liquid inertia effects. At the moment a constant value of 0.5 is used, which was found to be valid for inviscid flows and intermediate particle Reynolds numbers (Auton et al. , 1988; Magnaudet et al. , 1995).

2.1.3 Two-phase turbulence modeling

Apart from the above equations and models, the turbulent eddy viscosity is needed to close the Reynolds shear stress and turbulent dispersion terms. According to current baseline model descriptions, the dispersed gas phase is assumed to be laminar, while the liquid turbulence is taken into account by using the $k-\omega$ SST model (Liao et al. , 2015, 2019). The turbulence transfer at the interfaces, so-called bubble-induced turbulence, is considered through additional source terms in the turbulence transport equations.

$$\frac{\partial}{\partial \mathrm{t}}(\alpha_{\mathrm{L}}\rho_{\mathrm{L}}\mathrm{k_L}) + \nabla\cdot(\alpha_{\mathrm{L}}\rho_{\mathrm{L}}\boldsymbol{u}_{\mathrm{L}}\mathrm{k_L}) = \nabla\cdot[\alpha_{\mathrm{L}}(\mu_{\mathrm{L}}^{\mathrm{mol}} + \frac{\mu_{\mathrm{L}}^{\mathrm{turb}}}{\sigma_{\mathrm{k3}}})\nabla\mathrm{k_L}] + \alpha_{\mathrm{L}}\mathrm{P_k} - \beta'\alpha_{\mathrm{L}}\rho_{\mathrm{L}}\mathrm{k_L}\omega_{\mathrm{L}} + \mathrm{S_k} \tag{15}$$

$$\begin{aligned}\frac{\partial}{\partial \mathrm{t}}(\alpha_{\mathrm{L}}\rho_{\mathrm{L}}\omega_{\mathrm{L}}) + \nabla\cdot(\alpha_{\mathrm{L}}\rho_{\mathrm{L}}\boldsymbol{u}_{\mathrm{L}}\omega_{\mathrm{L}}) = \nabla\cdot[\alpha_{\mathrm{L}}(\mu_{\mathrm{L}}^{\mathrm{mol}} + \frac{\mu_{\mathrm{L}}^{\mathrm{turb}}}{\sigma_{\omega 3}})\nabla\omega_{\mathrm{L}}] + (1-\mathrm{F_1})2\alpha_{\mathrm{L}}\rho_{\mathrm{L}}\frac{\nabla\mathrm{k_L}\nabla\omega_{\mathrm{L}}}{\sigma_{\omega 2}\omega_{\mathrm{L}}} \\ +\mathrm{a_3}\alpha_{\mathrm{L}}\frac{\omega_{\mathrm{L}}}{\mathrm{k_L}}\mathrm{P_k} - \beta_3\alpha_{\mathrm{L}}\rho_{\mathrm{L}}\mathrm{k_L}\omega_{\mathrm{L}}^2 + \mathrm{S}_\omega\end{aligned} \tag{16}$$

Wherein P_k denotes the production rate of turbulence by liquid shear. The production limiter is activated, i.e.

$$\mathrm{P_k} = \min\left(\mu_{\mathrm{L}}^{\mathrm{turb}}\mathrm{S}^2, \mathrm{P_{lim}}\rho_{\mathrm{L}}\epsilon\right), \tag{17}$$

and the clip factor P_{lim} has a default value of 10. The formulation for the eddy viscosity is given by

$$\mu_{\mathrm{L}}^{\mathrm{turb}} = \frac{\mathrm{a_1}\rho_{\mathrm{L}}\mathrm{k_L}}{\max(\mathrm{a_1}\omega,\ \mathrm{SF_2})} \tag{18}$$

In the above equations σ_{k3}, β', $\sigma_{\omega 3}$, $\sigma_{\omega 2}$, a_1, a_3, β_3 are standard $k-\omega$ SST model constants, where k_L is turbulent kinetic energy, ω_L is turbulent eddy frequency of the liquid phase and F_1, F_2 are the first and second blending function, respectively, and S is an invariant measure of the strain rate. The source terms S_k and S_ω, accounting for turbulence generation and destruction due to the presence of bubbles, are determined according to the following model which was derived recently by Ma et al. (2017) based on the turbulence kinetic energy budget analysis of DNS data for turbulent bubbly channel flows (Santarelli et al. , 2016). It is commonly accepted that the kinetic energy production due to the relative motion between bubbles and liquid can be approximated as follows (Pfleger et al. , 2001; Politano et al. , 2003; Yao and Morel , 2004):

$$\mathrm{S_k} = \mathrm{C_k}\boldsymbol{F}_{\mathrm{D}}\cdot(\boldsymbol{u}_{\mathrm{G}} - \boldsymbol{u}_{\mathrm{L}}) \tag{19}$$

and the dissipation rate of the bubble-induced turbulence is often derived by analogy to the single-phase turbulence theory, namely, by introducing a characteristic time scale for quantification of energy dissipation as:

$$\mathrm{S}_\epsilon = \mathrm{C}_\epsilon\frac{\mathrm{S_k}}{\tau} \tag{20}$$

Accordingly, the relation between k_L, ϵ_L and ω_L, $\epsilon_L = \beta' k_L\omega_L$, leads to the computation of the ω source term as

$$\mathrm{S}_\omega = \frac{1}{\beta'\mathrm{k_L}}\mathrm{S}_\epsilon - \frac{\omega_{\mathrm{L}}}{\mathrm{k_L}}\mathrm{S_k} \tag{21}$$

Available bubble-induced turbulence models differ in defining the coefficients C_k, C_ϵ and the time scale τ Liao et al. (2019), where single-phase theories and dimensional analyses are often resorted

to. Ma et al. (2017) make a step forward and calibrate these quantities with help of laboratory and DNS results. They first select a time scale characterizing bubble-induced turbulence based on the temporal spectra of liquid velocity from DNS (Roghair et al. , 2011) and experiment (Mercado et al. , 2010) of bubbly flow, and then calibrate each term in the turbulence transport equations (Eqs.15 and 16) using DNS data (Santarelli et al. , 2016). The final expressions are given by

$$\mathrm{C_k} = \min\left(0.18\,\mathrm{Re_p}^{0.23},\ 1\right), \tag{22}$$

$$\mathrm{C}_\epsilon = 0.3\,\mathrm{C_D}, \tag{23}$$

$$\tau = \frac{\mathrm{d_B}}{|\boldsymbol{u}_\mathrm{G} - \boldsymbol{u}_\mathrm{L}|}. \tag{24}$$

As explained in the introduction, the baseline model is dedicated to turbulent bubbly flows, and numerous cases have been simulated with it (Rzehak et al. , 2017; Liao et al. , 2018, 2019). In the present work, the focus is set on low Reynolds number flows. The suitability of $k-\omega$ SST model for laminar single-phase pipe flows, and the capability of bubble-induced turbulence model in capturing velocity fluctuations in a homogeneous bubble column will be checked firstly. They will be then used for a series of laminar bubbly flows in a vertical pipe. A similar approach has been adopted by Marfaing et al. (2017) to simulate low Re bubbly flows and for comparison they use the experimental data of Nakoryakov et al. (1996). They neglected viscous and Reynolds shear stresses in the gas phase momentum equation, and modelled liquid Reynolds shear stresses making use of the standard $R_{ij}-\epsilon$ model of the NEPTUNE_CFD code but without consideration of bubble-induced turbulence, although the liquid velocity fluctuations are wholly due to the presence and motion of bubbles.

2.2 Numerics

Besides the closure models, numerics involved in solving the partial differential equations plays a crucial role in obtaining converged and reliable simulation results. For our case, we are using the PIMPLE solution algorithm which combines both the PISO (Pressure Implicit with Splitting of Operator) and SIMPLE (Semi-Implicit Method for Pressure-Linked Equations) method. The PIMPLE algorithm is just like SIMPLE loop but with outer correctors for every time step. This gives better stability over the PISO algorithm. Hence, PIMPLE loop requires the user to specify outer corrector loops for number of SIMPLE iterations to perform. For outer correctors equal to 1 the solution algorithm operates in PISO mode and for 2 or more than that it operates in SIMPLE mode. Further, the convergence of the simulation is checked by monitoring the temporal course of courant number and equation residuals. To summarize, the linearized Navier Stokes equation written in operator form as described in Kornev (2013) is:

$$u = Au + Bp + C \tag{25}$$

here A and B are corresponding coefficients of velocity and pressure terms.
With the SIMPLE method, the solution is seeking at each time step in form of the loop:

- Calculation of the auxiliary velocity:

$$u^* = Au^* + Bp^{(m-1)} + C, \tag{26}$$

- Calculation of the pressure correction:

$$\nabla Bp' = -\nabla u^*, \tag{27}$$

- Calculation of the velocity correction:

$$u' = Bp', \tag{28}$$

- Final correction for single iteration:

$$u^m = u^* + u', p^{(m)} = p^{(m-1)} + p'. \tag{29}$$

Here, m denotes the number of inner loops or the outer correctors in OpenFOAM. In our simulations, we specified the outer correctors as 3. So, for every time step the solver will perform 3 correction iterations and then will proceed to the next time step.

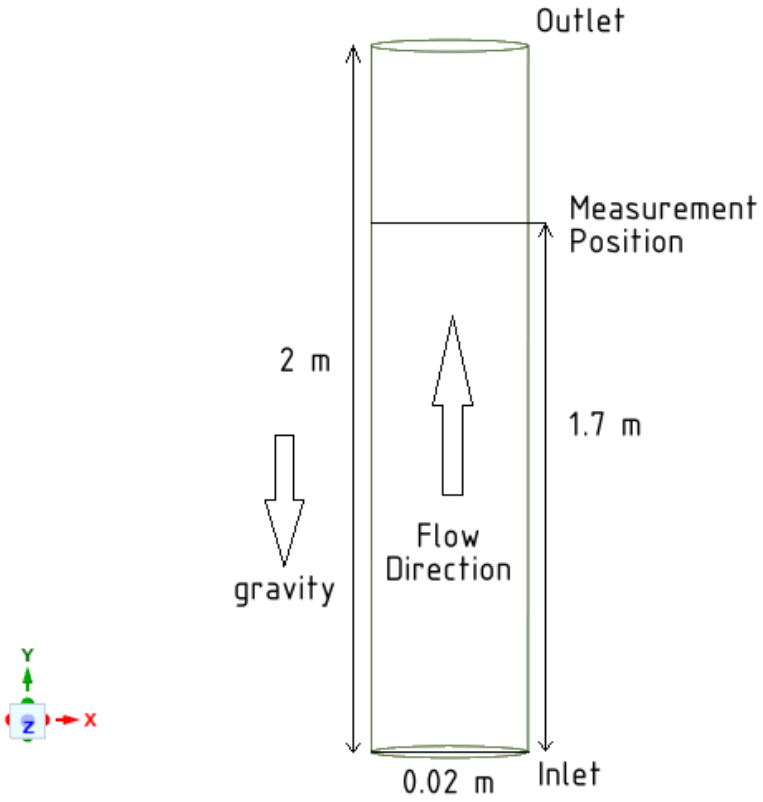

Figure 1: Sketch of the vertical test section and measurement position in Hosokawa and Tomiyama (2013) cases.

3 Experimental Summary

The simulations have been performed on a total of eight laminar bubbly flow cases, and data for comparison purposes are taken from Hosokawa and Tomiyama (2013) and Kim et al. (2016). The experimental conditions are summarized in Table 1, and a brief description of the experimental methods and procedures is given below.

Case No.	Pipe Diameter	J_L	J_G	Bubble Diameter (d_B)	Void Fraction (α_G)
	mm	m/s	m/s	mm	%
H1	20	4.5×10^{-2}	0.4×10^{-3}	3.48	0.18
H2	20	4.5×10^{-2}	1.6×10^{-3}	3.52	0.71
H3	20	4.5×10^{-2}	3.6×10^{-3}	3.59	1.56
H4	20	4.5×10^{-2}	3.0×10^{-3}	2.62	1.27
K1	40	1.88×10^{-2}	3.95×10^{-4}	2.2	0.05
K2	40	1.88×10^{-2}	6.05×10^{-4}	2.7	0.10
K3	40	1.88×10^{-2}	8.41×10^{-4}	3.1	0.17
K4	40	1.88×10^{-2}	2.44×10^{-3}	3.7	0.64

Table 1: Experimental data for test cases.

The Hosokawa and Tomiyama cases are one among the low liquid Reynolds number flows with Reynolds number as low as 900. The experimental setup is described in detail in Hosokawa and Tomiyama (2013). Water and air are fed into a vertical pipe of 20 mm diameter and 2 m height at room temperature and atmospheric pressure, see Figure 1. The injection device has been optimized to produce bubbly flows with more or less uniformly bubble size.

The flow conditions are varied to observe the "laminar" bubbly flow behavior precisely. Mainly, the gas volumetric flux and bubble diameter are altered and divided into combination of 4 possible

cases. Air void distribution, mean liquid velocity, mean bubble velocity, turbulent kinetic energy and Reynolds shear stress were measured radially at an axial distance of 1.7 m from the bottom, where the flow is considered to be quasi-fully developed. The cases are presented in Table 1 with letter "H".

Kim et al. (2016) performed similar experiments on "laminar" bubbly pipe flows with Reynolds number as 750. The measurements were taken in a vertical pipe of 40 mm diameter and 1.75 m height. Three positions were selected for measurements based on the characteristic of flow from developing to fully-developed i.e. z/D = 4.5, 21, 42 respectively. The data are recorded for radial profiles of void fraction, liquid velocity, bubble velocity and root mean square of velocity fluctuation at these three positions. In this work we focus on the fully-developed regime, and comparisons are only made for the upper position, i.e. z/D = 42. The uncertainties in the measured liquid velocity, bubble velocity, void fraction, bubble diameter and aspect ratio are given in Table 2. The cases are outlined in Table 1 with letter "K".

Measured Field	**Uncertainty (%)**
Vertical liquid velocity	0.05
Radial liquid velocity	5
Vertical gas velocity	2.5
Void fraction	3.7
Bubble diameter	6.5
Aspect ratio	3.7

Table 2: Measurement uncertainties present in Kim et al. (2016) cases.

Furthermore, the material properties used for air and water in all the simulations are tabulated in Table 3, which are in accordance with the experimental conditions.

Property (unit)	**Air**	**Water**
Density (kg/m^3)	1.185	998
Dynamic Viscosity (kg/m/s)	1.831×10^{-5}	8.899×10^{-4}
Surface Tension (N/m)	0.072	

Table 3: Material properties for air and water at room temperature.

Except the pipe diameter both the experiments were carried out at comparatively low Reynolds number and similar flow properties including the bubble-generating and air-water mixing devices. However, a difference lies in the profiles of the fields measured is observed. The radial profiles of void fraction, mean bubble and water velocity, and turbulence kinetic energy are plotted in Figure 2 and 3, respectively. A general comparison between the experimental observations is given in Table 4.

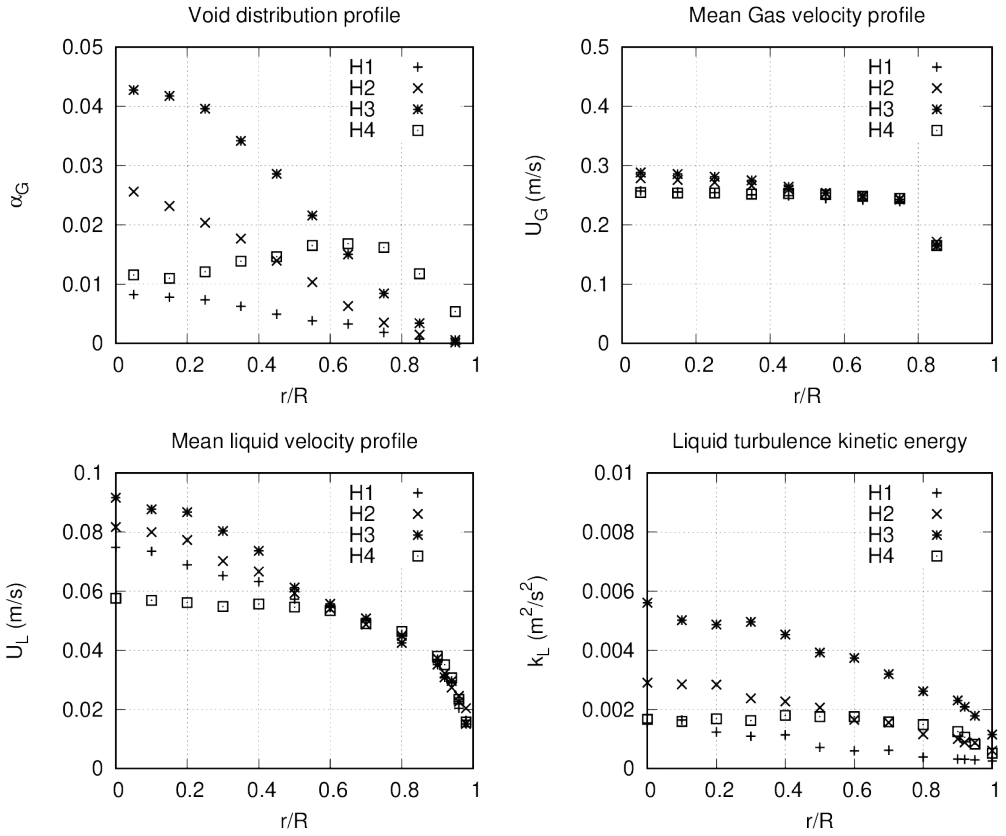

Figure 2: Variation of experimental results for different Hosokawa and Tomiyama (2013) cases.

Hosokawa and Tomiyama (2013)	Kim et al. (2016)
Void fraction	
Clear core-peaking void fraction profiles are observed in cases H1 to H3 while wall-peaking in case H4.	The void fraction profiles are flattened but wall-peaking in cases K1 to K3 while intermediate core-peaking in case K4.
Bubble velocity	
With increasing gas flux the mean bubble rising velocity also increases (very slowly) for same bubble diameter and decreases rapidly for smaller diameter.	With increasing gas flux, the mean bubble velocity decreases from cases K1 to K4, although the bubble diameter increases.
Liquid velocity	
With increasing gas flux the liquid velocity increases for case H1, H2 and H3 but decreases again for case H4.	With increasing gas flux the liquid velocity also increases from cases K1 to K4.
Bubble diameter	
The gas flux in cases H1, H2, H3 increases while bubble diameter is kept constant around 3.5 mm. In case H4 the gas flux is kept between H2 and H3 but the bubble diameter is clearly lesser than other 3 cases.	Bubble diameter increases with the gas flux from case K1 to K4.

Table 4: A general comparison between observations of considered cases from literature.

As discussed above the relative motion of bubbles is the main source of velocity fluctuations in

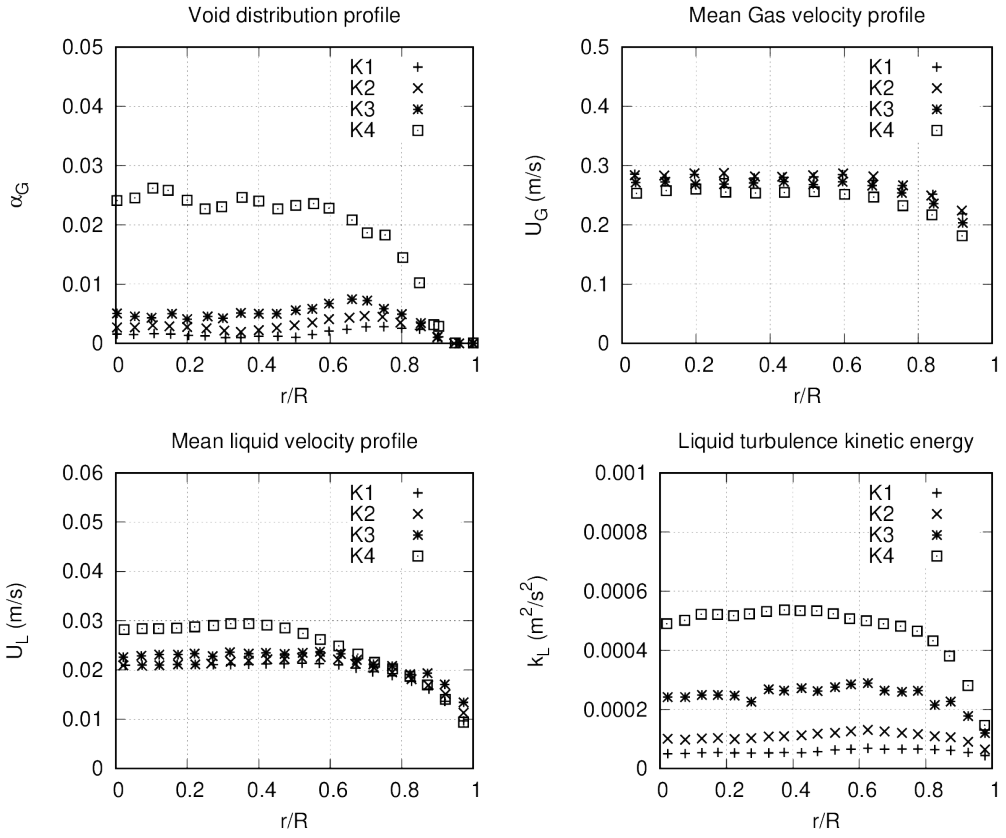

Figure 3: Variation of experimental results for different Kim et al. (2016) cases.

Grid	$N_{radial}(x)$	$N_{axial}(y)$	Δ_x (mm)	Δ_y (mm)	N_{total}
Coarse	10	100	1.0	20.0	1000
Medium	20	200	0.5	10.0	4000
Fine	40	400	0.25	5.0	16000

Table 5: Grid size distribution for Hosokawa and Tomiyama (2013) cases.

these cases. Figure 4 compares the measured bubble terminal velocity with the ones predicted by some widely-used drag models. The Bozzano and Dente (2001) model over-estimates the terminal velocity in all cases. The Tomiyama et al. (1998) model for pure and contaminated systems and the Ishii and Zuber (1979) model are able to give reasonable predictions for the Kim et al. (2016) cases. The bubble terminal velocity measured by Hosokawa and Tomiyama (2013) is noticeably lower, and all models fail to reproduce it. The correlation proposed by Ishii and Zuber (1979) is adopted in the present work.

4 Simulation Setup and Sensitivity Study

4.1 Geometry and Mesh

For high computational efficiency, a wedge of the pipe with a small angle of 2.5° instead of the whole pipe is simulated. The simplification is reasonable as the flow is axisymmetric (mirrored around the axis). For the small wedge a quasi 2D mesh is applied, i.e. one layer of cells in the azimuthal direction, and the two cut faces are treated as symmetrical planes, see Figure 5.

To achieve mesh-independent results, mesh studies are performed for three uniform grid resolutions. Table 5 and Table 6 denotes the grid sizes with total number of cells and cell size for each. The mesh-study results for the cases H4 and K4 are shown in Figure 6 and Figure 7, respectively.

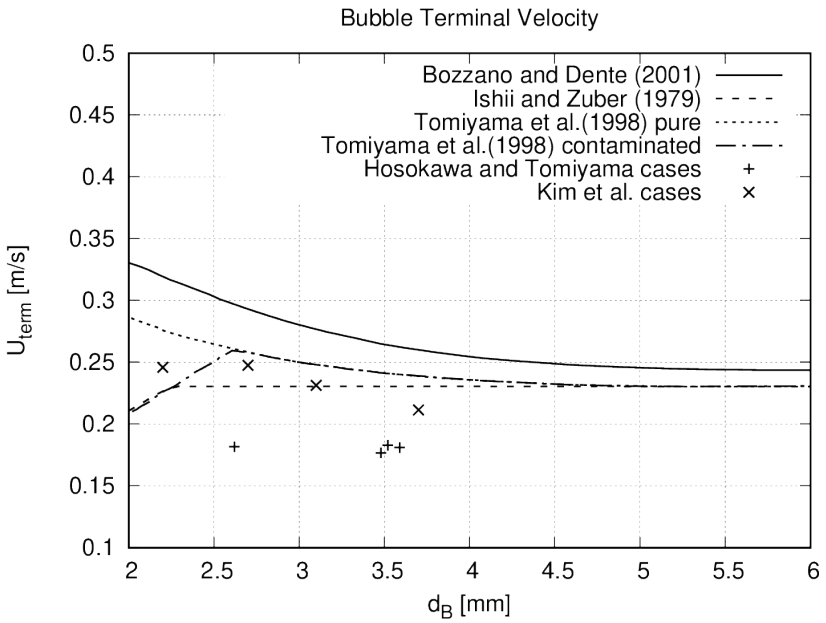

Figure 4: Comparison of measured bubble terminal velocity with model predictions.

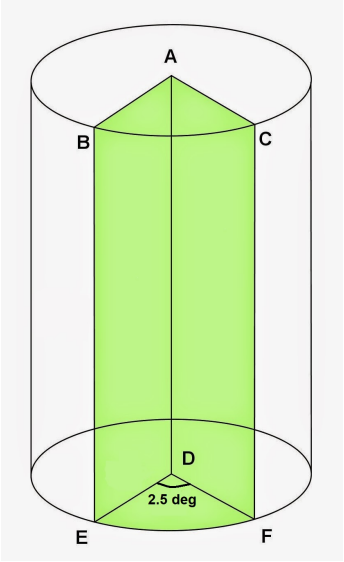

Figure 5: Pipe channel used in simulations.

Grid	$N_{radial}(x)$	$N_{axial}(y)$	Δ_x (mm)	Δ_y (mm)	N_{total}
Coarse	20	100	1.0	20.0	2000
Medium	40	200	0.5	10.0	8000
Fine	80	400	0.25	5.0	32000

Table 6: Grid size distribution for Kim et al. (2016) cases.

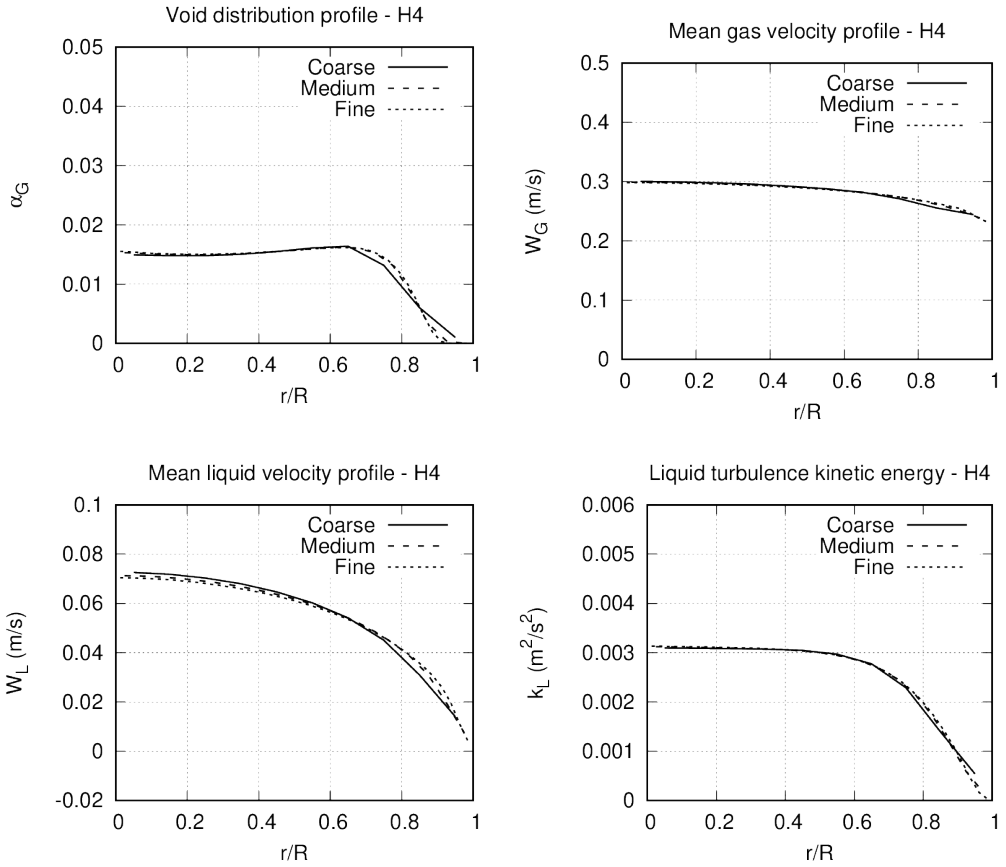

Figure 6: Mesh-study results for Hosokawa and Tomiyama (2013) case (H4).

Void fraction, gas and liquid mean velocity and turbulent kinetic energy are compared. As seen from the results, no major difference is noticed. Only slight deviation exists near the wall especially in the Hosokawa and Tomiyama cases, which were conducted in a smaller pipe. The results obtained using the medium mesh can be already considered as mesh-independent. Consequently, we choose the coarse mesh for the subsequent simulation of our cases.

4.2 Boundary Conditions

Beside the wedge boundary conditions applied for the front and back planes, boundary conditions are needed for the inlet, outlet and wall of the domain. Flow direction is vertically upwards against the gravity with a uniform constant value at the inlet. Both air and water are entering from the same wedge inlet with a pre-defined volume fraction calculated using the correlation:

$$\alpha_G = \frac{J_G}{J_G + J_L} \tag{30}$$

$$\alpha_L = 1 - \alpha_G \tag{31}$$

by assuming zero slip velocity, where gas flux (J_G) and liquid flux (J_L) are specified by the experimental conditions. Accordingly, inlet values for velocity fields are calculated using:

$$U_G = \frac{J_G}{\alpha_G} \tag{32a}$$

$$U_L = \frac{J_L}{\alpha_L} \tag{32b}$$

The inlet conditions for turbulence parameters k and ω are determined by using the relation:

$$k = \frac{3}{2}(U_L I)^2 \tag{33}$$

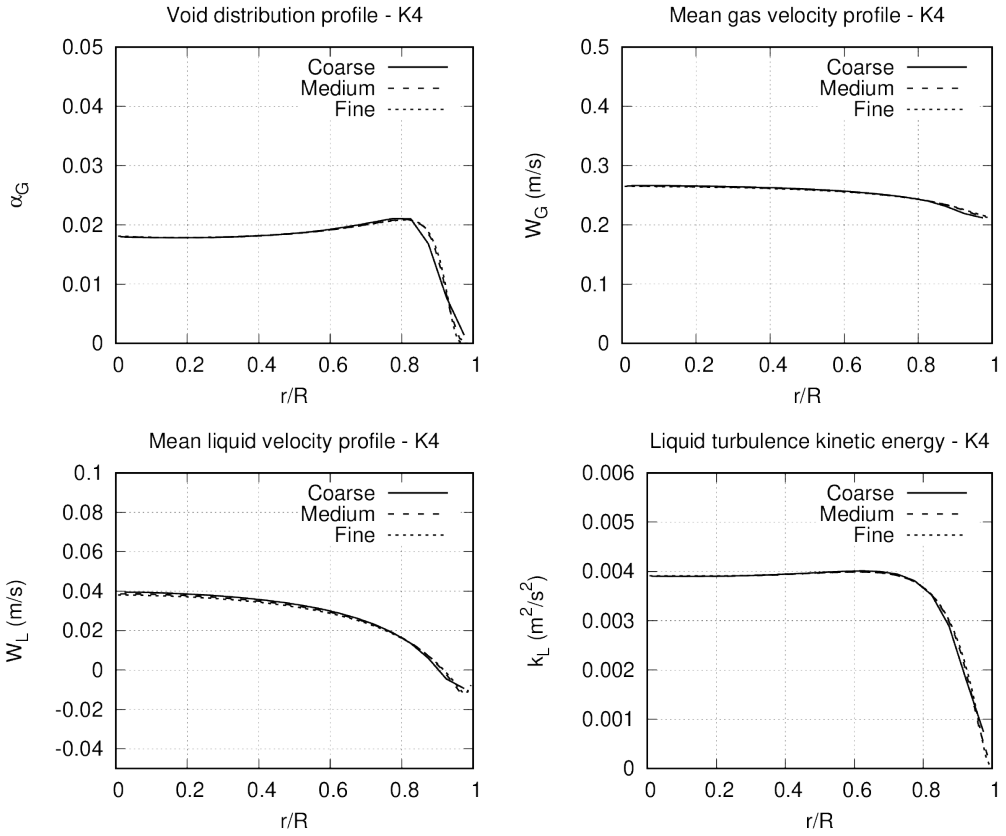

Figure 7: Mesh-study results for Kim et al. (2016) case (K4).

and,

$$\omega = \frac{\sqrt[2]{k}}{C_\mu L} \tag{34}$$

where I is the turbulence intensity which is estimated as 1 % for flows with low turbulence. The turbulent length scale, L is in the range of 10 to 20 % of pipe diameter, and L = 0.1D is assumed in the present study. Further, the inlet boundary conditions for velocity and turbulence are found to have negligible effect on the fully-developed field profiles of interest, which are determined by the flow rates and bubble diameter. As an overview, boundary conditions for all fields at inlet, outlet and walls are tabulated in Table 7.

4.3 Pre-Processing

For carrying out the simulations we have used a solver derived from reacting multi-phase Euler foam which takes care of solving all the pre-requisite models discussed above. The solver

Field/ Patch	Internal Field	Inlet	Outlet	Walls
α_G	0	from cases	Neumann	Neumann
k_{water}	k_{in}	Dirichlet	inletOutlet	Wall Function
ω_{water}	ω_{in}	Dirichlet	inletOutlet	Wall Function
P	1×10^5	calculated	calculated	calculated
P_{rgh}	1×10^5	Neumann	Dirichlet	fixedFluxPressure
U_{air}	0	from cases	Neumann	slip
U_{water}	0	from cases	Neumann	noSlip

Table 7: Boundary conditions used in simulation set-up.

is developed at HZDR and is named as HZDRreactingMultiPhaseEulerFoam, where the baseline closures described above are available. The solver uses the finite volume method with first order discretization scheme in time and second order in space. For solving the pressure-velocity coupled equations, SIMPLE method is used. The flow is simulated for 20 seconds to get a steady state solution at which a strict convergence of residuals is obtained.

5 Results

The following section compares the experimental and simulation results. The experimental data is extracted from the paper using a digital software and is plotted along with results from OpenFOAM for a general comparison. The plots are self-explanatory. It is necessary to note that the model setup is validated beforehand for two single-phase laminar flows, which represent the bulk flow in the Hosokawa and Tomiyama (2013) and Kim et al. (2016) cases, respectively. The predicted mean velocity profiles conform with the analytical parabolic ones, which indicates that the $k-\omega$ SST model is applicable for low-Re single-phase flows. Whether it is capable of capturing the transition from laminar to turbulent flow due to bubble injection by including bubble-induced source terms will be discussed below.

5.1 Hosokawa and Tomiyama cases

The prediction of air volume fraction for the Hosokawa and Tomiyama cases is plotted in Figure 8. It has an obvious deviation from the experimental values in cases H1 to H3 but confirms nicely for case H4. In the former three cases large volume fractions are measured at the center of the pipe, and the core peak increases with the air fluxes. In contrast, the simulations predict a transition profile between wall-peak and core-peak ones, and thus a significant underestimation of the void fraction observed at the pipe center. Nevertheless, the agreement between experiment and simulation in case H4 is excellent in the whole cross section. The major difference between the case H4 and other three cases is having a smaller bubble diameter (see Table 1). As mentioned above, among other non-drag forces the shear-induced lift force plays a crucial role in forming a core- or wall-peak profile of the void distribution in vertical pipe flows. The lift force coefficient is dependent on bubble size and shape, and may change from positive to negative at some cross-over point, which is around $5.6\,mm$ according to the Tomiyama model (Tomiyama et al. , 2002). The fact is known that the cross-over value may be different in different fluid systems, since bubble deformation and shape are sensitive to fluid properties and impurities. In case 4 the Tomiyama model seems to provide a reasonable lift force coefficient C_L resulting in a intermediate peak as observed. A similar C_L value and void fraction profile are predicted by the model for cases H1 to H3. The deviation from the measurements implies that under the experimental conditions the cross-over point of lift force coefficient may occur already between 2.6 mm and 3.5 mm and bubbles having a size around 3.5 mm experience a negative lift force (pointing to velocity gradient direction) and migrate to the pipe center. Similar discussions have been given by Ekambara et al. (2012) for horizontal pipe flows. To achieve the measured gas volume fraction profile, they needed a negative lift coefficient for the bubbles in the size range of 2-3 mm, and thus proposed a correlation to be a function of particle Reynolds number instead of the Eötvös number as given by the Tomiyama correlation. Further investigation towards a general lift coefficient for bubbly flow is needed.
It is evident in Figure 9 that the predicted vertical gas velocity is slightly higher than the measured ones in all the four cases. The deviation is supposed to be related to the prediction of drag force and terminal velocity. As shown in Figure 4 the Ishii-Zuber correlation adopted in this work is prone to over-predict the terminal velocity in these cases. It is widely accepted that surfactants and impurities in the liquid have an effect on the terminal rise velocity of bubbles. For example, bubbles in the size range of d_B=0.5-20 mm rise more slowly in contaminated water than in pure water. It may be an indication that the tap water used in the Hosokawa and Tomiyama (2013) experiments was heavily contaminated, and the drag coefficient is under-predicted by the Ishii and Zuber (1979) drag model. Overall, the results for radial gas velocity profiles are in good agreement with the experimental data, and difference in the magnitude is within an acceptable range.

Figure 10 outlines the comparison for vertical liquid velocity, which shows a satisfying agreement between the experimental and simulation values in case H1. A very slight under-prediction is seen near the wall of the pipe, but overall the plots are nicely confirming. Furthermore, the model is tested beforehand for the single water flow with a mean velocity of 4.5×10^{-2} m/s, which is equal

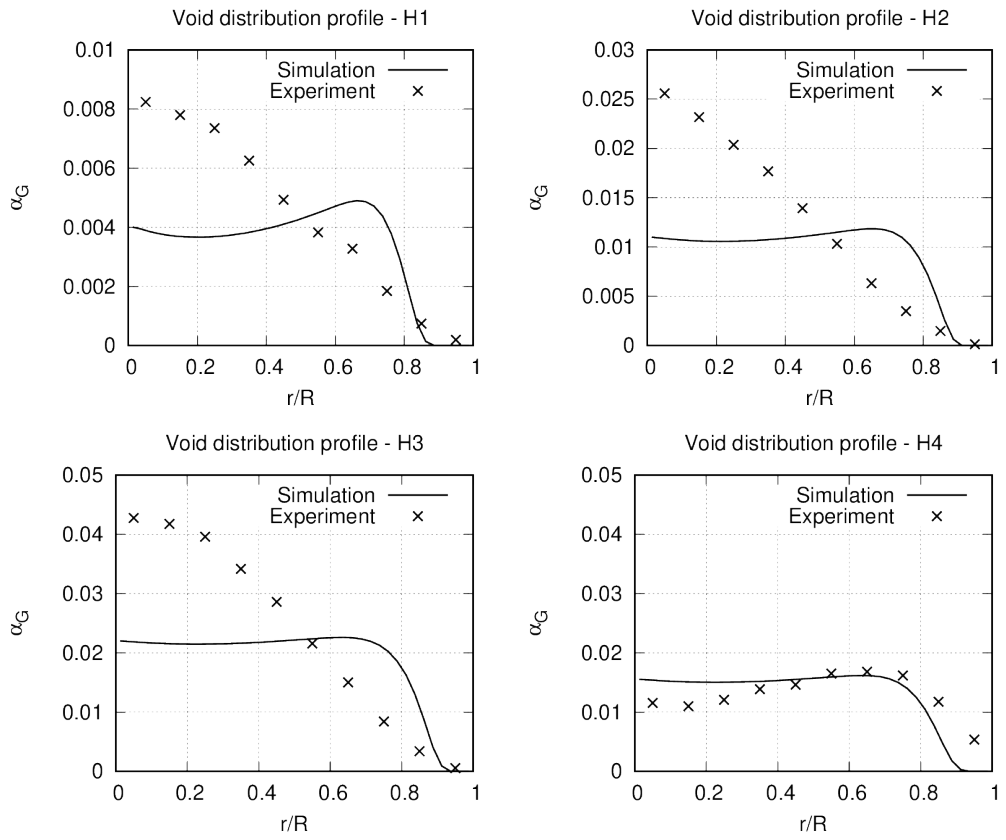

Figure 8: Comparison between simulated and measured gas volume fraction for Hosokawa and Tomiyama (2013) cases.

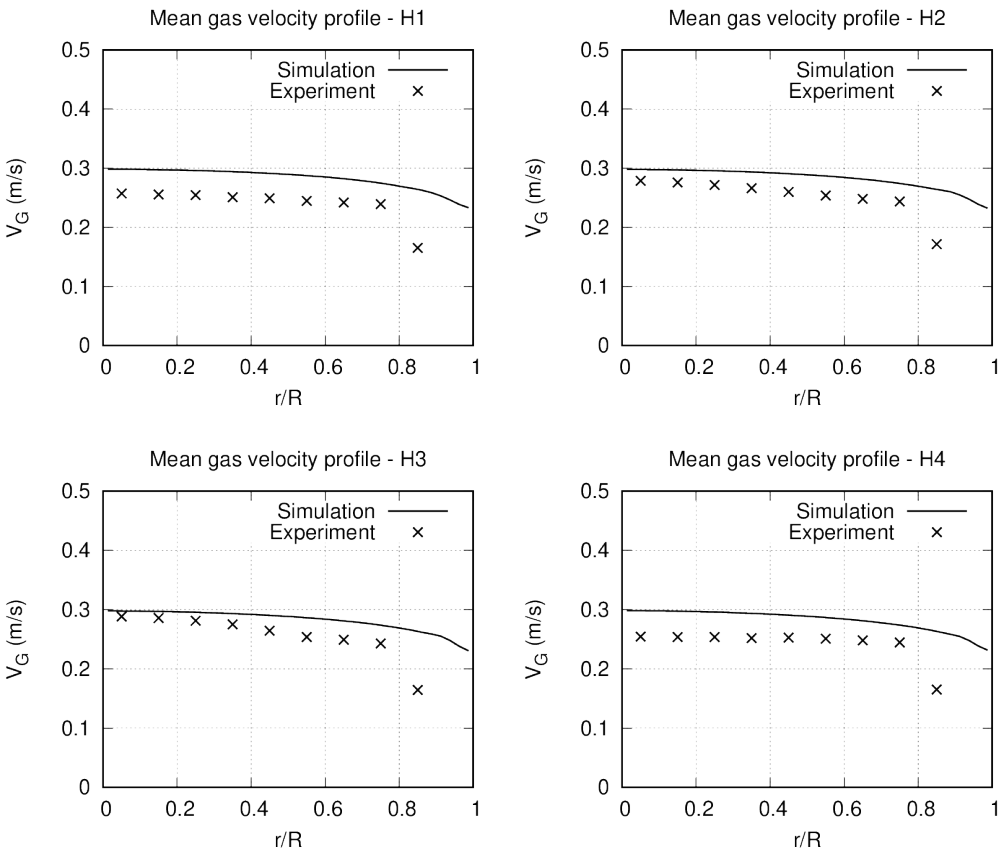

Figure 9: Comparison between simulated and measured vertical gas velocity for Hosokawa and Tomiyama (2013) cases .

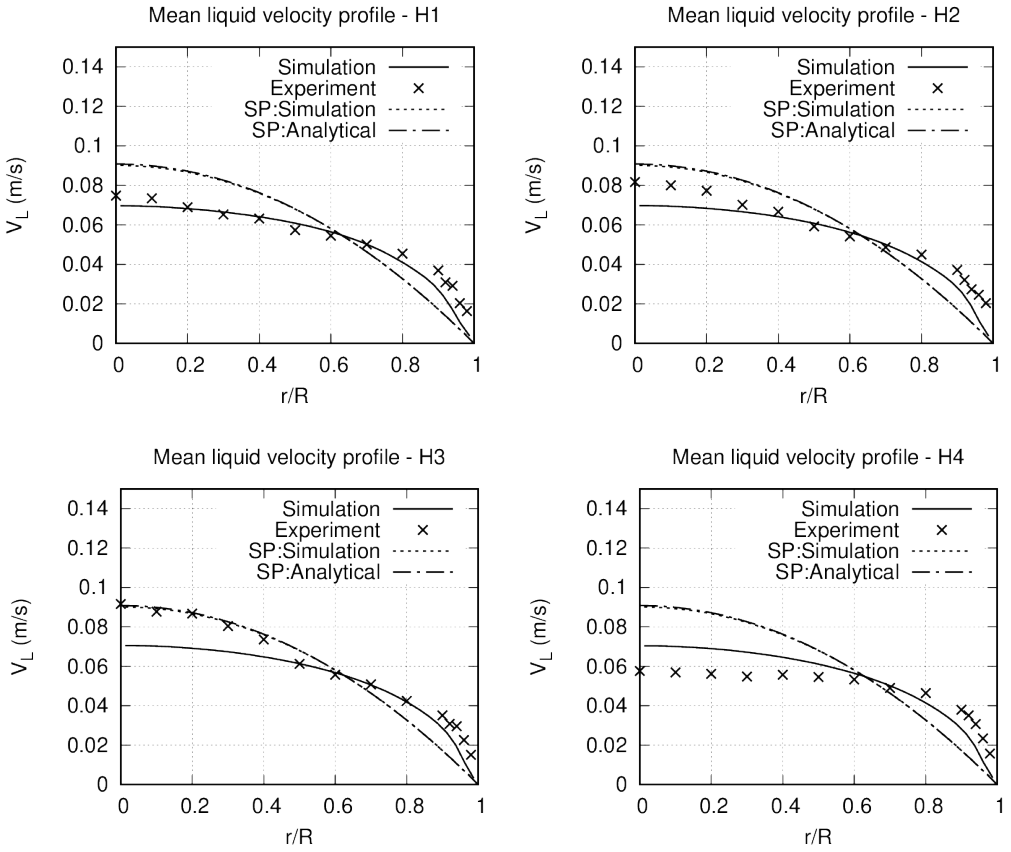

Figure 10: Comparison between simulated and measured vertical liquid velocity for Hosokawa and Tomiyama (2013) cases.

to the liquid volumetric flux of the bubbly flow cases. The vertical velocity is plotted in Figure 10 as a reference, which is named "SP:Simulation" in the legend, and "SP:Analytical" represents the analytical parabolic velocity profile for laminar flow. The applied turbulence model is evidenced to work well in the single-phase laminar flow. It is interesting to see that the measured velocity in cases H2 and H3 takes a mixed up lateral profile, namely, laminar in the center region while turbulent near the wall of the pipe. One can speculate that the cases are located in the laminar-turbulent transition region, which seems to be challenging for the baseline model. In the case of H4 a typical turbulent velocity profile is measured, which conforms with the numerical results. Since the bubble size in H4 is relatively small in comparison to other cases, it may indicate that under the investigated conditions, e.g. void fraction and bubble size, the transition from laminar to turbulent profiles is expedited at large pipe-to-bubble size ratios. It is inconsistent with the experimental results on the effect of neutrally-buoyant suspended particles published by Matas et al. (2003).

The plots of turbulent kinetic energy in Figure 11 are similar to those of air void fraction as outlined by the authors in Hosokawa and Tomiyama (2013). The deviation in the pipe center region is mainly due to the under-prediction of void fraction as discussed above. The radial distribution in case H4 is well captured by the model, but the value is obviously higher than the measured one. Possible explanation is the over-prediction of the relative velocity, since the bubble-induced turbulence production rate is proportional to $|\boldsymbol{u_G} - \boldsymbol{u_L}|^3$. Nevertheless, the prediction and measurement are in the same order of magnitude in all four cases.

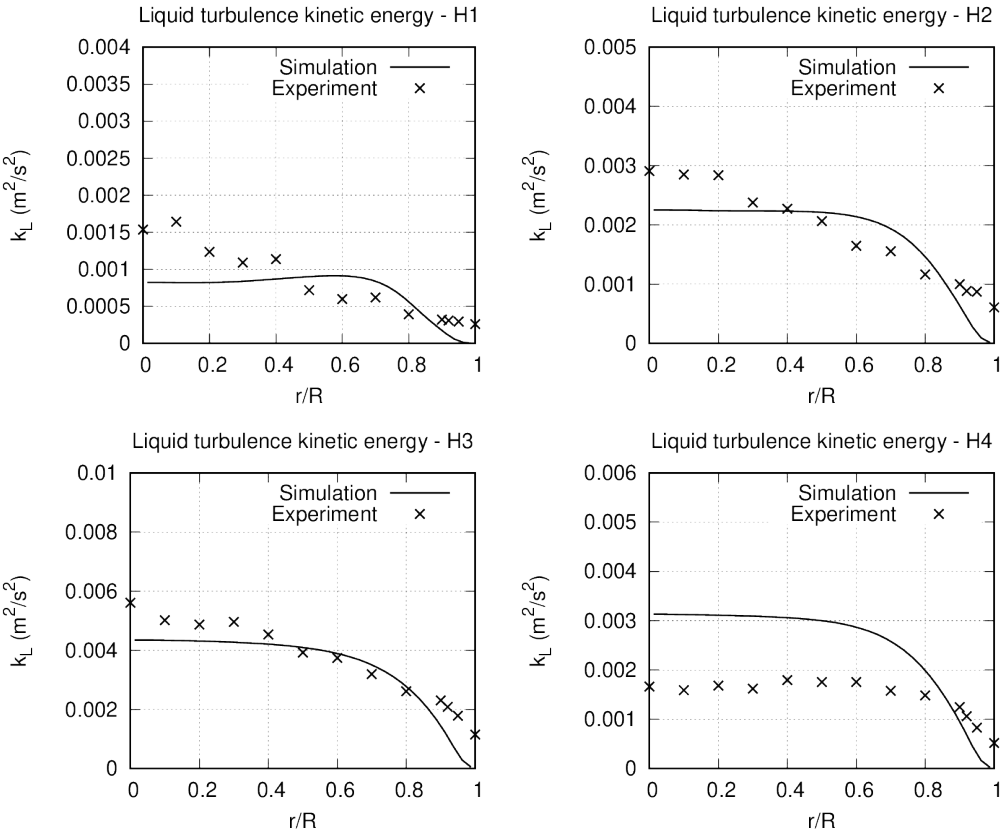

Figure 11: Comparison between simulated and measured turbulent kinetic energy for Hosokawa and Tomiyama (2013) cases.

For examining the prediction of eddy viscosity as well as the Boussinesq hypothesis, a measured shear stress ($\tau_B = -\rho(\overline{u'v'})$) is considered for comparison. This could be correlated with equation 4 as:

$$\boldsymbol{\tau_B} = \rho\mu_L^{turb}(\frac{\partial v}{\partial x} + \frac{\partial u}{\partial y}) \tag{35}$$

As seen in Figure 12, the plots follow the same profile, and in case H4 the values agree even very well with the measurement. Obvious under-prediction is present in cases H1 $\sim$ H3, where the turbulent kinetic energy is nevertheless well reproduced as shown in Figure 11. It might be an indication of an under-estimated eddy viscosity provided by the baseline model in the first three cases or inaccuracy of Boussinesq approximation for modelling the Reynolds stress. Under-prediction of eddy viscosity in bubbly flows by the baseline model has been discussed for high-Re cases in Liao et al. (2019). Although the current BIT model of Ma et al. (2017) performs better than that of Rzehak and Krepper (2003), which was included in the previous version of the baseline model, further efforts toward two-phase turbulence modelling especially the effect of bubbles are required. Furthermore, in the intermediate cases H1 to H3 the experiment observed a peak of Reynolds shear stress around $r/R = 0.5$ and relatively high stresses over the whole cross-section, while the simulation evidences the peak position of $r/R = 0.8$ and low stresses in the pipe center region. The profiles in the fully-developed turbulent case H4 are in a quantitatively and qualitatively good agreement.

5.2 Kim et al. cases

The same procedure is applied for the Kim et al. (2016) cases listed in Table 1. As contrast to Hosokawa and Tomiyama (2013) observations on the air void fraction for Kim et al. cases agree to much higher extent, see Figure 13. It is only in case 4 (K4) that some deviation is seen close to the center of the pipe, where the prediction is lower. As also mentioned above, the measured void fraction profiles in these cases are all relatively flat and have no significant peaks. It is quite

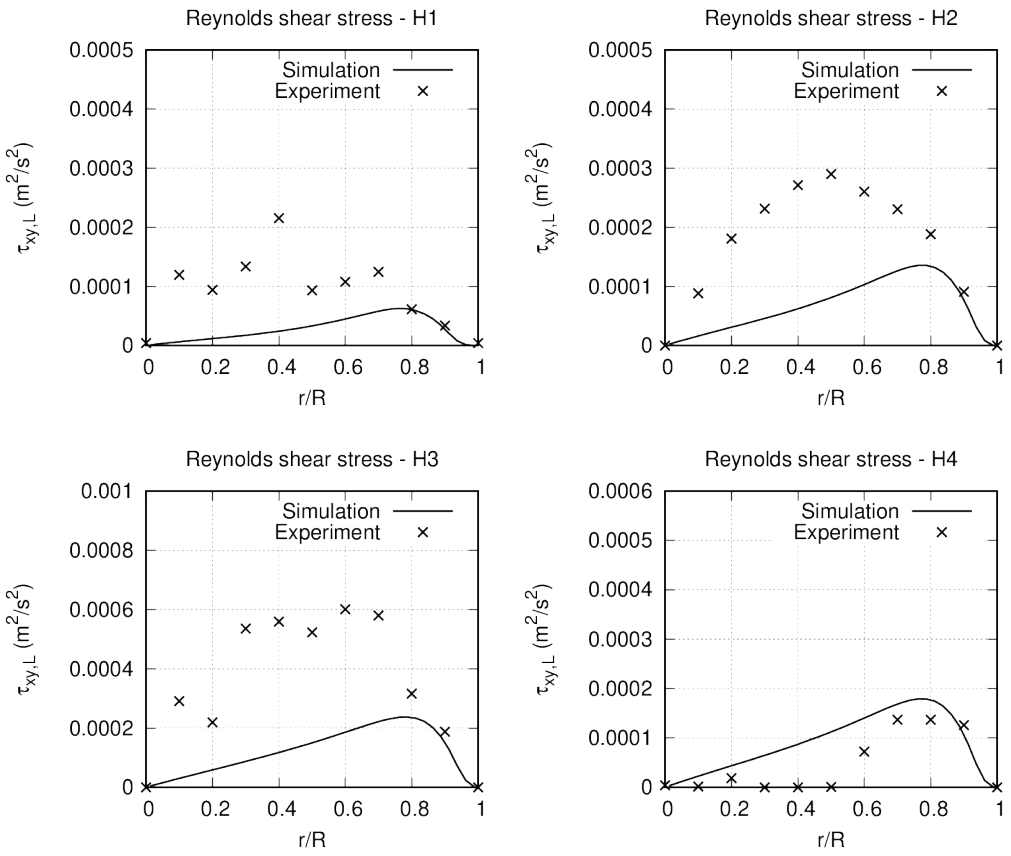

Figure 12: Comparison between simulation and experimental results for Reynolds shear stress (u'v') for Hosokawa and Tomiyama (2013) cases.

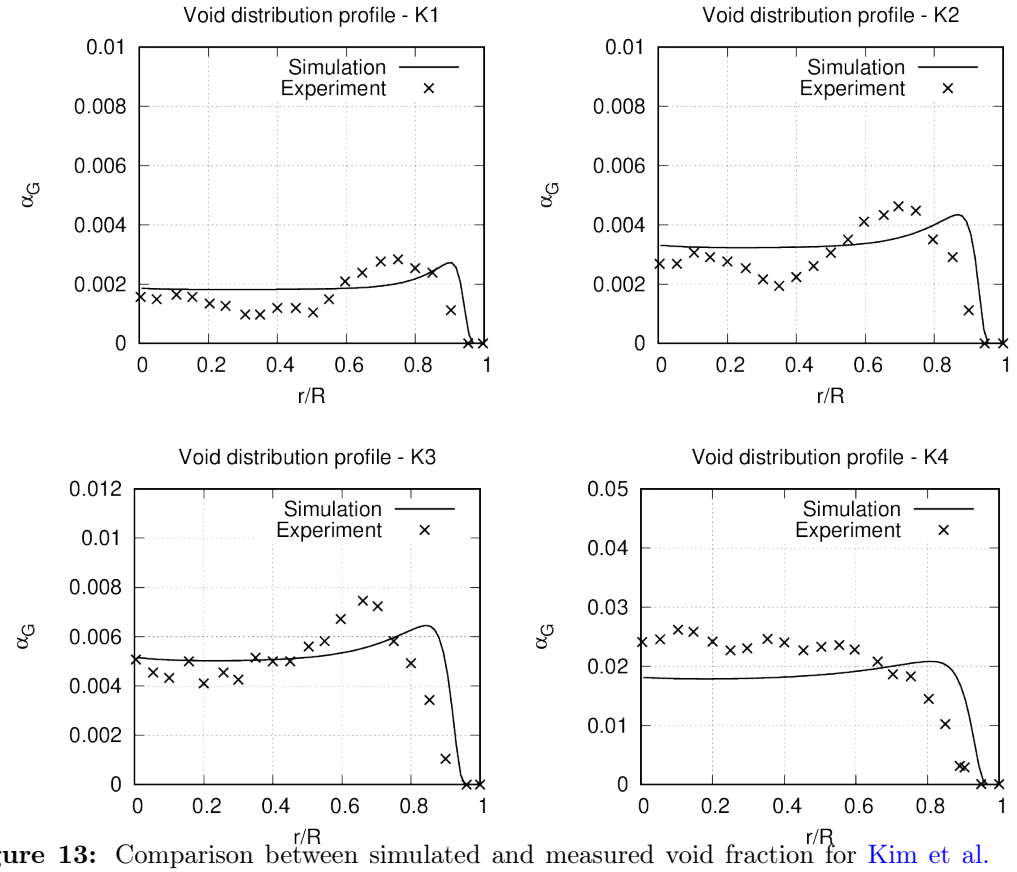

Figure 13: Comparison between simulated and measured void fraction for Kim et al. (2016) cases.

similar to the case H4, but deviates widely from the observations in the cases H1 $\sim$ H3. As in the case H4, the flow in the cases K1 to K4 is suspected to be fully-developed turbulent. It is consistent with the speculation that the critical point for the transition from laminar to turbulent is lower in larger pipes. Actually, flat void fraction profile in large pipes at high Re conditions has been discussed by Shawkat et al. (2008) and Ohnuki and Akimoto (2001). They assumed that turbulent dispersion plays a more important role in larger pipes. Although it is not widely recognized, the observations of Hosokawa and Tomiyama (2013),Kim et al. (2016), Shawkat et al. (2008), Ohnuki and Akimoto (2001) and Matas et al. (2003) confirm that the pipe-to-bubble size has an effect on the turbulence structure, intensity as well as the transition in bubbly flows. Nevertheless, the flat profile measured by Kim et al. (2016) conforms with the prediction of the baseline model in this work.

In contrast to an overall over-prediction in the Hosokawa and Tomiyama (2013) cases, a slight under-prediction of the mean gas velocity is observed in cases K1 and K2. Nevertheless, a completely good agreement between the simulation and measurement is achieved for case 3 and 4 (see Figure 14). This is consistent with the prediction of the bubble terminal velocity and drag coefficient presented in Figure 4.

The mean liquid velocity is in perfect agreement with the experimental results in the single phase and fully-developed turbulent case K1, see Figure 15. As the gas flux increases from K1 to K4, both the mean void fraction and the bubble size increase. According to the measurement, the vertical liquid velocity remains unchanged in the former three cases and a slight but almost homogeneous increase in latter case. On the other hand, a continuous increasing trend is obtained in the numerical analysis. Consequently, the liquid velocity in the center region is higher than the experimental data while near the pipe wall lower. Because of the quite velocity, in the case K4 negative value even appears in the simulation results. As discussed above, the major difference between the two laminar bubbly flow experiments is the diameter of the test section. Since the pipe in this experiment is twice as large as that in Hosokawa and Tomiyama (2013), the mean velocity is lower at comparable Reynolds numbers and in the center region almost four times lower (see Figures 10 and 15).

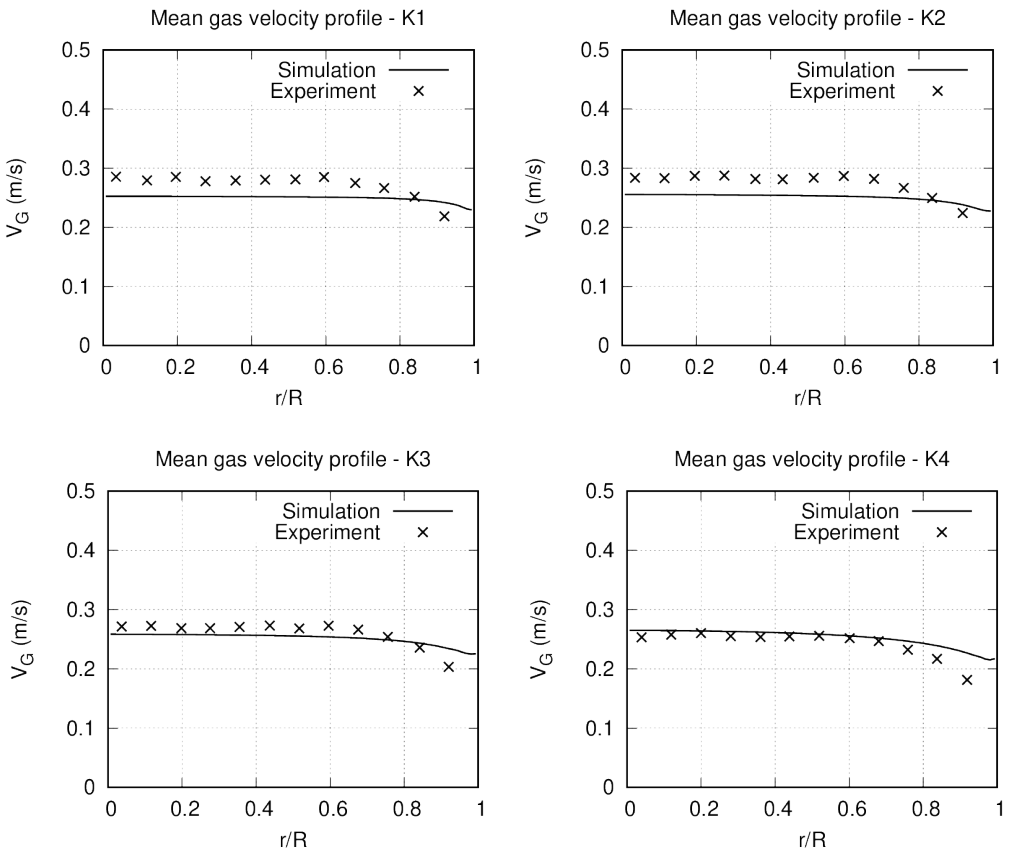

Figure 14: Comparison between simulated and measured vertical gas velocity for Kim et al. (2016).

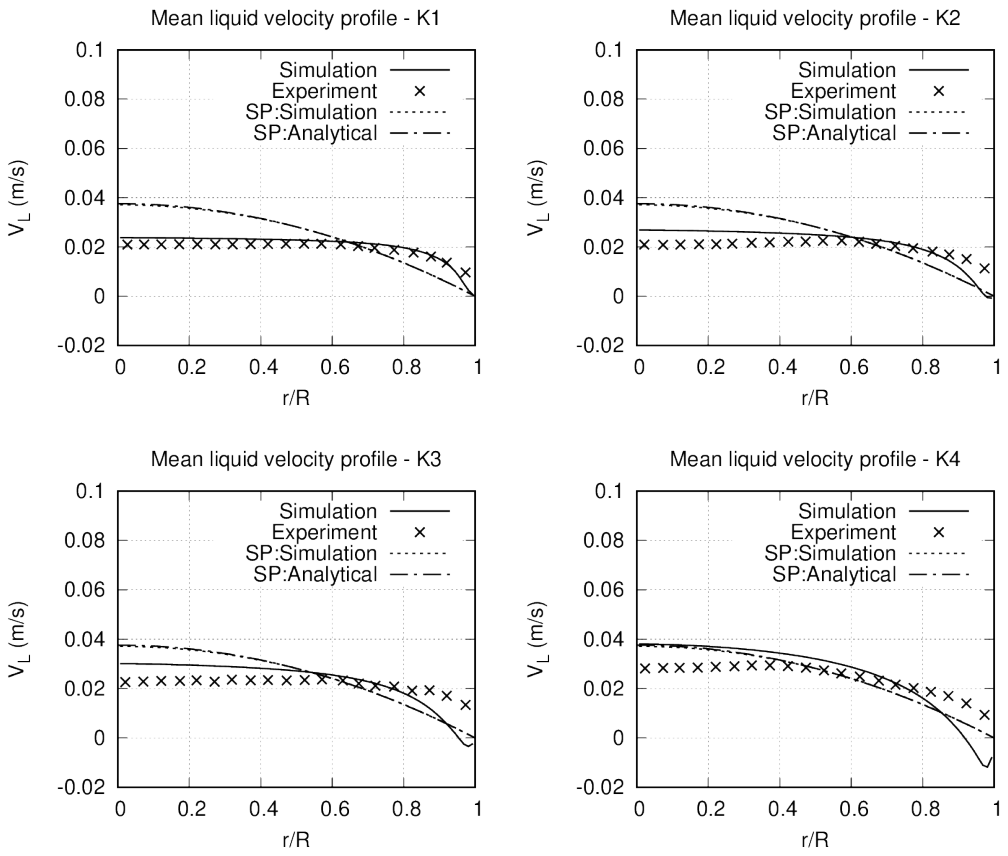

Figure 15: Comparison between simulated and measured vertical liquid velocity for Kim et al. (2016) cases.

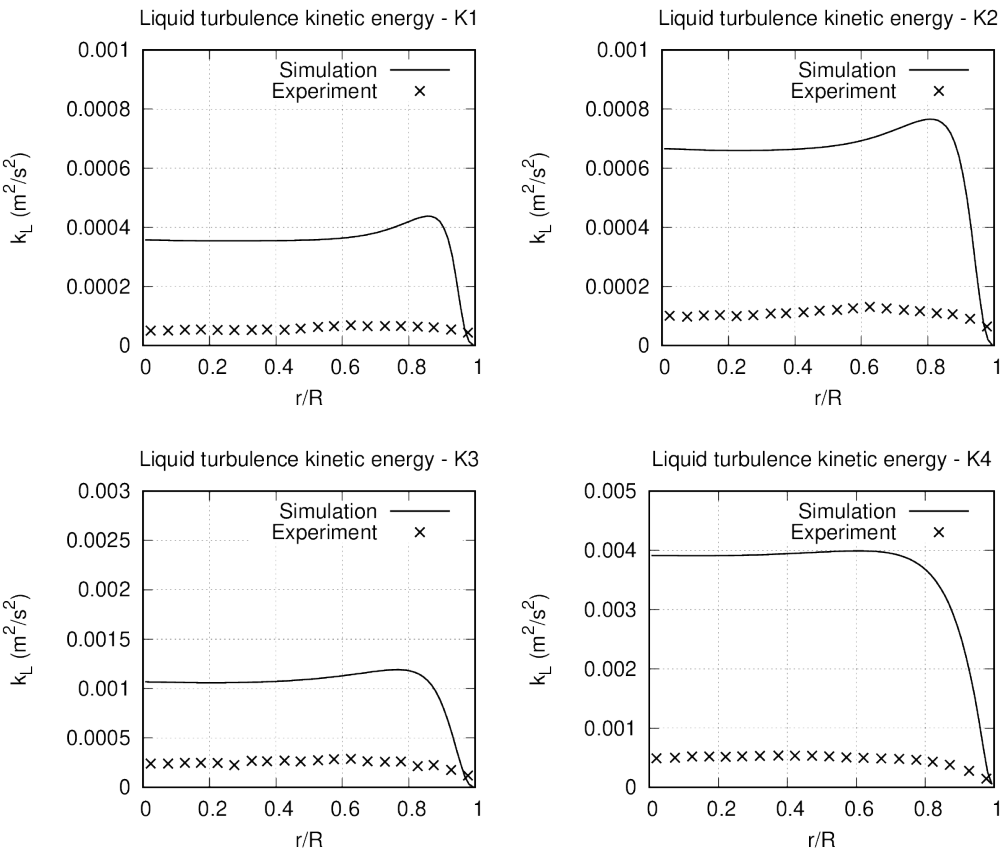

Figure 16: Comparison between simulated and measured turbulent kinetic energy for Kim et al. (2016) cases.

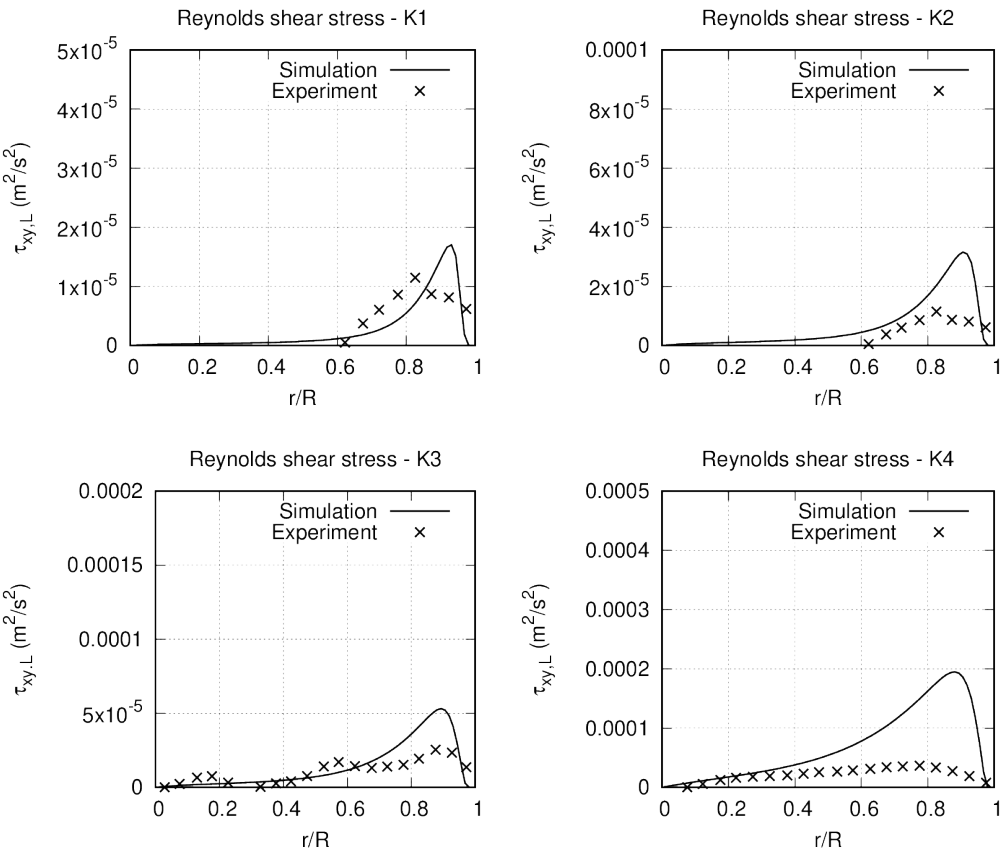

Figure 17: Comparison between simulated and measured Reynolds shear stress for Kim et al. (2016) cases.

Comparison results for turbulent kinetic energy are outlined in Figure 14. It shows that the turbulent kinetic energy is one order of magnitude lower than that in the Hosokawa and Tomiyama (2013) cases. Like in case H4 significant over-prediction by the numerical model is observed in all the four cases. It proves that the baseline model tends to over-predict the turbulent kinetic energy in fully-developed turbulent bubbly flows in small to medium pipes, although confirming results for the transition cases are achieved as shown in Figure 11. Consequently in Figure 15, Reynolds shear stress is also plotted. The shear stress shows a relatively better conformance with experimental results, which has also been evidenced for the case H4 in Figure 12.

6 Conclusion

In comparison to turbulent bubbly flow, "laminar" bubbly flow has received much less attention. Little is known about the mechanism of the transition from "laminar" to "turbulent" due to the infusion of bubbles. Reliable prediction of hydrodynamics and interfacial transfer processes is still challenging, and assessment of existing models and approaches is necessary. In this work the Euler-Euler two-fluid approach incorporated with the baseline model is applied and evaluated for these cases in the OpenFOAM library. The HZDR baseline model that serves as a basis for digging out as much as possible the insufficiency in existing models has been applied to a relatively large number of turbulent bubbly flows. In this work, its applicability in low-Re cases, where bubble-induced turbulence is dominant, is tested for eight different set of flow conditions from two experimental databases which mainly differ in pipe diameter. Being an open source toolbox, OpenFOAM offers great flexibility for this kind of closure test and comparison simulations. The solver used in the simulations is developed at HZDR for the special purpose of testing the baseline model. For a fair comparison, efforts have been made to replicate as far as possible the experimental conditions in simulations, e.g. by choosing an appropriate grid and material properties, maintaining gas and liquid flow rates and mean bubble diameter. Numerical error is minimized by choosing high-order algorithms, strict convergence criteria and doing mesh-Independence studies. The sampling of data fields from simulations is made carefully in accordance to the experimental procedure. The obtained predictions for air volume fraction, liquid and gas velocity, and turbulence parameters are all in the same magnitude as the experimental data provided by Hosokawa and Tomiyama (2013) and Kim et al. (2016). To assist understanding of the flows and further polishing of the baseline model, following conclusions are drawn:

- The pipe-to-bubble size ratio has an influence on the threshold for bubbles bring the flow from laminar to turbulent;
- In laminar or transitional flows bubbles having a size around 3.5 mm prefer to be accumulated in the pipe center, which is much smaller than the value of 5.6 mm given by Tomiyama (2002) with consideration of the lift effect. The mechanism besides the lift force driving bubbles towards to pipe center is unclear;
- The baseline model for Euler-Euler two-fluid modelling of bubbly flows predict the phase distribution well in fully-developed turbulent cases, but fails in reproducing the core-peak profile measured in laminar and transitional cases, e.g. H1, H2 and H3;
- The model tends to give over-prediction of the vertical liquid velocity in the pipe center while under-prediction in the near-wall region. It is challenging to reproduce the profiles in cases with low bulk velocity and high gas void fraction, e.g. K3 and K4;

  The model gives perfect prediction of velocity profile for single-phase laminar flows as well as extremely sparse bubbly flows, e.g. H1 and K1;
- Inconsistencies are observed in matching the turbulence parameters. In cases with conforming turbulent kinetic energy the Reynolds shear stress is overall under-predicted, while turbulent kinetic energy is over-predicted if Reynolds shear stress is reproduced.

Further investigation on the mechanism of turbulence region growing, laminar-turbulent transition, transfer between bubbles and the bulk is of general interest.

References

Nakoryakov, V. E., Kashinsky, O. N., Randin, V. V., Timkin, L. S. (1996). Gas-liquid bubbly flow in vertical pipes. Journal of Fluids Engineering, 118, 377-382.

Hosokawa, S., Tomiyama, A. (2013). Bubble-induced pseudo turbulence in laminar pipe flows. International Journal of Heat and Fluid Flow, 97-105.

Kim, M., Lee, J. H., Park, H. (2016). Study of bubble-induced turbulence in upward laminar bubbly pipe flows measured with a two-phase particle image velocimetry. Experiments in Fluids, 57, 55.

Tomiyama, A. (2002). Struggle with computational bubble dynamics. Thrid International Conference on Multiphase Flow, ICMF98, Lyon, France, June 8-12.

Lucas, D., Tomiyama, A. (2011). On the role of the lateral lift force in poly-dispersed bubbly flows. International Journal of Multiphase Flow, 37, 1178-1190.

Lucas, D., Rzehak, R., Krepper, E., Ziegenhein, Th., Liao, Y., Kriebitzsch, S., Apanasevich, P. (2016). A strategy for the qualification of multi-fluid approaches for nuclear reactor safety. Nuclear Engineering and Design, 299, 2-11

Liao, Y., Rzehak, R., Lucas, D., Krepper, E. (2015). Baseline closure model for dispersed bubbly flow: bubble coalescence and breakup. Chemical Engineering Science, 122, 336-349

Liao, Y., Lucas, D. (2016). Poly-disperse simulation of condensing steam-water flow inside a large vertical pipe. International Journal of Thermal Sciences, 104, 194-207

Rzehak, R., Ziegenhein, T., Kriebitzsch, S., Krepper, E., Lucas, D. (2017). Unified modeling of bubbly flows in pipes, bubble columns, and airlift columns. Chemical Engineering Science, 157, 147-158

Liao, Y., Ma, T., Liu, L., Ziegenhein, Th., Krepper, E., Lucas, D. (2018). Eulerian modeling of turbulent bubbly flow based on a baseline closure concept. Nuclear Engineering and Design, 337, 450-459

Kriebitzsch, S., Rzehak, R. (2016). Baseline Model for Bubbly Flows: Simulation of Monodisperse Flow in Pipes of Different Diameters. Fluids, 1, 29

Ishii, M., Zuber, N. (1979). Drag coefficient and relative velocity in bubbly, droplet or particulate flows. American Institute of Chemical Engineers, 843–855.

Saffman, P.G. (1965). The lift on a small sphere in a slow shear flow. Journal of Fluid Mechanics, 22, 385-400.

Tomiyama, A., Tamai, H., Zun, I., Hosokawa, S. (2002). Transverse migration of single bubbles in simple shear flows. Chemical Science Engineering, 1849–1858.

Wellek, R. M., Agrawal, A. K., Skelland, A. H. P. (1966). Shapes of liquid drops moving in liquid media. A.I.Ch.E. Journal, 12, 854–862.

Hosokawa, S., Tomiyama, A., Misaki, S., Hamada, T. (2002). Lateral migration of single bubbles due to the presence of wall. ASME Joint U.S.-European Fluids Engineering Division Conference. Montreal.

Antal, S. P., Lahey Jr., R.T., Flaherty, J.E. (1991). Analysis of phase distribution in fully developed laminar bubbly two-phase flow. International Journal of Multiphase Flow, 17, 635-652.

Burns, A., Frank, T., Hamill, I., Shi, J.-M. (2001). The Favre averaged drag model for turbulence dispersion in Eulerian multi-phase flows. 5th International Conference on Multiphase Flow (ICMF 2004). Yokohama, Japan.

Auton, T., Hunt, J., Prud'Homme, M. (1988). The force exerted on a body in inviscid unsteady non-uniform rotational flow. Journal of Fluid Mechanics, 197, 241-257.

Magnaudet, J., Rivero, M., Fabre, J. (1995). Accelerated flows past a rigid sphere or a spherical bubble Part 1: Steady straining flow. Journal of Fluid Mechanics, 284, 97-135.

Ma, T., Santarelli, C., Ziegenhein, T., Lucas, D., Fröhlich, J. (2017). Direct numerical simulation–based Reynolds-averaged closure for bubble-induced turbulence. Phys. Rev. Fluids 2, 034301.

Marfaing, O., Laviéville, J. (2017). Bubble force balance formula for low Reynolds number bubbly flows in pipes and channels: comparison of wall force models. International Journal of Chemical Reactor Engineering, 2017, 1-16.

Ekambara, K., Sanders Sean, R., Nandakumar, K., Masliyah., J.H. (2012). CFD modeling of gas-liquid bubbly flow in horizontal pipes: influence of bubble coalescence and breakup. International Journal of Chemical Engineering, 2012, 1-20.

Kornev, N. (2013). Computational Methods of Heat and Mass Transfer. Faculty of Mechanical Engineering and Marine Technology, Chair of Modelling and Simulation, 2013, 58-73.

Liao, Y., Ma, T., Krepper, E., Lucas, D., Fröhlich, J. (2019). Application of a novel model for bubble-induced turbulence to bubbly flows in containers and vertical pipes. Chemical Engineering Science, 202, 55-69.

Santarelli, C., Fröhlich, J. (2016). Direct numerical simulations of spherical bubbles in vertical turbulent channel flow: Influence of bubble size and bidispersity. International Journal of Multiphase Flow, 81, 27-45.

Pfleger, D., Becker, S. (2001). Modelling and simulation of the dynamic flow behaviour in a bubble column. Chemical Engineering and Science, 56, 1737-1747.

Politano, M.S., Carrica, P. M., Converti, J. (2003). A model for turbulent polydisperse two-phase flow in vertical channels. International Journal of Multiphase flow, 29, 1153-1182.

Yao, W., Morel, C. (2004). Volumetric interfacial area prediction in upward bubbly two-phase flow. International Journal of Heat and Mass Transfer, 47, 307-328.

Roghair, I., Mercado, J. M., Van Sint Annaland, M., Kuipers, H., Sun, C., Lohse, D. (2011). Energy spectra and bubble velocity distributions in pseudo-turbulence: Numerical simulations vs. experiments. Int. J. Multiphase Flow, 37, 1093-1098.

Mercado, J. M., Gómez D. C., van Gils, D., Sun, C., Lohse, D. (2010). On bubble clustering and energy spectra in pseudo-turbulence. J. Fluid Mech., 650, 287-306.

Ziegenhein, T., Lucas, D. (2017). Obervations on bubble shapes in bubble columns under different flow conditions. Experimental Thermal and Fluid Scinece, 85, 248-256.

Tomiyama, A., Kataoka, I., Zun, I., Sakaguchi, T. (1998). Drag Coefficients of single bubbles under normal and micro gravity conditions. JSME Int. J. Ser. B, 41, 472-479.

Bozzano, G., Dente, M. (2001). Shape and terminal velocity of single bubble motion: a novel approach. Comput. Chem. Eng., 25, 571–576.

Rzehak, R., Krepper, E. (2013). CFD modeling of bubble-induced turbulence. Int. J. Multiph. Flow, 55, 138–155.

Shawkat, M., Ching, C.Y., Shoukri, M. (2008). Bubble and liquid turbulence characteristics. Int. J. Multiph. Flow, 34, 767–785.

Ohnuki, A., Akimoto, H. (2001). Model development for bubble turbulent diffusion and bubble diameter in large vertical pipes. J. Nucl. Sci. Technol., 38,1074–7080.

Matas, J.-P., Morris, J.F., Guazzelli, $\acute{E}$. (2003). Transition to turbulence in particulate pipe flow. Phys. Rev. Lett. 90, 014501